COMMUNICATIONS IN COMPUTATIONAL PHYSICS
Vol. **6**, No. 4, pp. 673-698

Commun. Comput. Phys.
October 2009

Computational Investigation of the Effects of Sample Geometry on the Superconducting-Normal Phase Boundary and Vortex-Antivortex States in Mesoscopic Superconductors

Sangbum Kim[1,*], Max Gunzburger[2], Janet Peterson[2] and Chia-Ren Hu[3]

[1] *Division of Energy Systems Research, Ajou University, Suwon 442-749, Korea.*
[2] *Department of Scientific Computing, Florida State University, Tallahassee, FL 32309-4120, USA.*
[3] *Center for Theoretical Physics, Department of Physics, Texas A&M University, College Station, Texas 77843, USA.*

Received 23 November 2008; Accepted (in revised version) 29 December 2008

Available online 5 March 2009

Abstract. A computational study of superconducting states near the superconducting-normal phase boundary in mesoscopic finite cylinders is presented. The computational approach uses a finite element method to find numerical solutions of the linearized Ginzburg-Landau equation for samples with various sizes, aspect ratios, and cross-sectional shapes, i.e., squares, triangles, circles, pentagons, and four star shapes. The vector potential is determined using a finite element method with two penalty terms to enforce the gauge conditions that the vector potential is solenoidal and its normal component vanishes at the surface(s) of the sample. The eigenvalue problem for the linearized Ginzburg-Landau equations with homogeneous Neumann boundary conditions is solved and used to construct the superconducting-normal phase boundary for each sample. Vortex-antivortex (V-AV) configurations for each sample that accurately reflect the discrete symmetry of each sample boundary were found through the computational approach. These V-AV configurations are realized just within the phase boundary in the magnetic field-temperature phase diagram. Comparisons are made between the results obtained for the different sample shapes.

AMS subject classifications: 58D19, 65N22, 65N25, 65N30

PACS: 79.60.Bm, 73.20.Dx, 74.72.-h

Key words: Superconductivity, nucleation, symmetry, finite element method.

*Corresponding author. *Email addresses:* sangbumkim@ajou.ac.kr (S. Kim), gunzburg@scs.fsu.edu (M. Gunzburger), peterson@scs.fsu.edu (J. Peterson), crhu@tamu.edu (C.-R. Hu)

1 Introduction

There are many important technological and fundamental questions concerning magnetic properties and superconducting states in superconductors of mesoscopic scale. Recent advances in microfabrication and experimental techniques have made possible extensive studies of such small systems. In this paper, we provide a computational study of some of these questions.

When the system is in the normal conducting state, the external magnetic field fully penetrates the system. At a temperature below a critical temperature T_c, as the applied magnetic field decreases, a superconducting state nucleates in the system. Knowing this critical level of the magnetic field, *i.e.*, the nucleation field, one can construct the normal/superconducting (N/S) phase boundary, if that transition is of second order.

As is well known, a bulk superconductor is called type-I when $\kappa < 1/\sqrt{2}$ and type-II for $\kappa > 1/\sqrt{2}$, where κ is the Ginzburg-Landau parameter. If $\kappa < 0.417$ [1, 2], we have the pure (homogeneous) superconducting state (the Meissner state) below the thermodynamic critical field H_c and the normal conducting state above H_c. For $0.417 < \kappa < 1/\sqrt{2}$, there exists a critical field H_{c3} such that a surface superconductivity state exists for $H_c < H < H_{c3}$ while the bulk of the sample remains in the normal conducting state; for $H > H_{c3}$, the whole sample is in the normal conducting state [1, 2].

For bulk type-II superconductors, we have a mixed state and the Abrikosov vortex lattice is energetically favorable in the range $H_{c1} < H < H_{c2}$ [2], where H_{c2} is called the upper critical field, and H_{c1}, the lower critical field. We have the Meissner state below H_{c1} and a surface superconductivity state for $H_{c2} < H < H_{c3}$.

For circular cylindrical samples, surface superconductivity nucleates in the form of a giant vortex (GV) [3, 4]. The order parameter takes the form $\psi = f(r)e^{iL\varphi}$, where the winding number L is a good quantum number; L is analogous to the orbital angular momentum of a particle. Calculations on the superconducting state in mesoscopic, type-I, superconducting thin films by solving the non-linear Gingzburg-Laudau equations (GL) at $H < H_{c2}$ have, in most cases, found transitions between GV states of different circulation quantum numbers L, with some multi-vortex (MV) states occasionally appearing as thermodynamically stable states, which become metastable below a critical radius [5–8]. Note that in general, L of a sample is defined as the sum of the winding numbers of all vortices minus the sum of the winding numbers of all antivortices in the sample, where the winding number of a vortex (antivortex) is defined to be the number of multiples of 2π (-2π) that the phase of the superconducting "pair-wave-function" order parameter ψ changes along a counterclockwise closed curve surrounding the vortex (antivortex).

As the size of sample becomes smaller and smaller, the geometry and topology of the sample has a fundamental influence on the superconducting state, and boundary effects increasingly dominate the nucleation of superconductivity.

The fluxoid quantization requirement gives rise to an oscillatory depression in the critical temperature T_c in cylindrical shells as described by the classical experiment of Little and Parks [9, 10]. One should also recall that in thin films, the parallel critical field

$H_{c||}(T)$ has a square-root ($\sim\sqrt{T_c-T}$) dependence [1, 11] and oscillations in the $T_c(H)$ phase boundary are superimposed on this parabolic background. More recently this oscillatory $T-H$ curve was obtained for simply connected domains such as a small disk [12] and a mesoscopic square [13, 17]. Oscillations arise from the change of the orbital angular momentum L as the imposed external magnetic flux Φ/Φ_0 increases [14], where $\Phi_0\equiv hc/2e$ denotes the flux quantum.

Moshchalkov *et al.* [13, 14] measured the H-T phase boundary of nucleation of superconductivity in aluminum samples (line, square, square loop) using resistance measurements and compared the results with the Tinkham formula for a thin slab and with solutions of the linearized Ginzburg-Landau (LGL) equation for disk and ring geometries. Fomin *et al.* [15, 16] built the phase boundary curve for a mesoscopic square loop with two leads by solving the full nonlinear Ginzburg-Landau equations in a self-consistent way near the critical temperature. A fitting parameter η which represents the fraction of superconducting area in the loop, was used to fit the measured curve of the resistive transition, which is based on the criterion $R/R_N=$ some constant <1, where R is the sample resistance in the superconducting-normal transition region and R_N is that for normal phase[†].

Bruyndoncx *et al.* [17] investigated the nucleation of superconductivity in a uniform perpendicular magnetic field in aluminum microsquares containing 2 and 4 antidots (holes). The normal/superconducting phase boundary for a square sample showed pseudoperiodic oscillations in $T_c(H)$ superimposed on an almost linear background. However, the $T_c(H)$ curve for a perforated microsquare displays a behavior reminiscent of superconducting network for low magnetic field, and indicates that a GV state is established in high magnetic fields. The influence of the actual geometries on $T_c(H)$ was studied in the framework of the LGL equation.

Jadallah *et al.* [18] computed the N/S phase transition curves for mesoscopic superconductors. Limiting shapes of the curves and asymptotic formulas for various orders of the applied magnetic flux were derived. It was shown that the fractional depression of the critical temperature, $(T_c-T)/T_c$, becomes linear with respect to the applied magnetic flux $\phi\equiv\Phi/\Phi_0$ for $\phi\gg1$, while $(T_c-T)/T_c$ shows a parabolic dependence on ϕ for low magnetic flux. The sensitivity of those results with respect to the smoothness of the

[†]The experimental phase boundary in the T-H plane can be defined in more than one ways: (i) By using the criterion $R(T,H)/R_N=$ some constant <1. (For example, it could be set at 0.5, 0.75, or 0.9, etc.) (ii) By fitting the high field part of the transition region of the resistance curve at a fixed T by a straight line, and then looking for its intersection with the horizontal line $R=R_N$. The field value at which this happens is defined as the critical field at this T. The phase boundary obtained with the first definition should be compared with the solution of the non-linear GL equations [better yet, with a direct calculation of $R(T,H)$, by solving, for example, a set of time-dependent GL equations]. After all, at any $R<R_N$, the strength of superconductivity must be already not infinitesimal, albeit still weak and inhomogeneous. On the other hand, the phase boundary obtained with the second definition should be compared with the solution of the linear GL equation, since R is practically already equal to R_N at this phase boundary, if not for the rounding of data due possibly to sample inhomogeneity and thermal fluctuations, which have all been neglected in the solution of the linear GL equation.

domain was studied.

Chibotaru *et al.* [19–23] investigated, using the LGL equation, the N/S phase boundary and vortex states in regular polygons (square, equilateral triangle, and rectangle, etc.) having discrete rotational symmetry. Note that each of these samples belongs to the C_4, C_3, and C_2 symmetry group, respectively. They found antivortices as well as vortices nucleate inside the samples studied subjected to uniform applied fields, and the vortex states preserved the discrete C_N symmetry of the sample boundary. They also found the phase-boundary (T_c-H) curve as the envelope of intersecting continuous curves of the lowest eigenvalues of different L of the irreducible representations (irreps) for each C_N symmetry group.

Kogan *et al.* [24] solved the *linearized* anisotropic GL equations to study the nucleation of superconductivity in anisotropic superconductors having an arbitrary orientation of the sample surface relative to the crystal principal axes. The surface critical field H_{c3} is found to be less than $1.695H_{c2}$ unless the field is situated along one of the principal crystal planes. Below H_{c3} in the vicinity of nucleation, the order parameter scales as $\sqrt{H_{c3}-H}$. Computational studies for infinite cylinders having rectangular cross sections were presented that showed that, due to corners and a finite cross section, the surface superconductivity state persists for fields above the theoretically predicted value for semi-infinite samples. They also showed that vortices exist within the surface superconductivity sheath above the bulk critical field.

In this paper, we solve the LGL equation with homogeneous Neumann boundary condition using a finite element method (FEM) in samples having various geometrical shapes. For an introduction to finite element discretizations of the GL equations, see, *e.g.*, [25,26]. Finite element methods are well known to be a powerful numerical method that are particularly suitable for the non-rectangular computational domains we consider. Our goal is to examine the effects of the geometric symmetry of the samples on the vortex states near the critical temperature T_c. In order to solve the LGL equations, the free boundary condition (see Eq. (2.2) below) must be satisfied. To reduce the boundary condition (BC) to a homogeneous Neumann BC, a vector potential gauge $\mathbf{A}$ satisfying $\mathbf{A}\cdot\mathbf{n}=0$ needs to be found. Since it is difficult to obtain analytical solutions satisfying this condition except for some standard, regular polygons, it is clear that FEMs can provide an effective alternative means for more complicated geometries. Although Chibotaru *et al.* [19–23] have developed an elegant analytic method to obtain the vector potential in a gauge in which $\mathbf{A}\cdot\mathbf{n}=0$ on the edge of a regular polygon sample, their symmetrized basis functions can handle only perfectly symmetric samples and not even slightest deviation from it is allowed. Even after their series of an infinite number of basis functions is truncated for computation, each remaining basis function is still perfectly symmetric. In other words, Chibotaru et al.'s method is programmed with everything perfectly symmetric, and it has yet to be non-trivially generalized in order to apply to samples of more complex geometries. To our knowledge, a numerical study of this kind even for a pentagon (which is still a simple polygon) has not yet been reported, which likely indicates that their method is not trivial to apply even for more complex polygons. Thus we

feel that there is a strong need to develop a new method to deal with more complex geometries (including more complex symmetric shapes, more general asymmetric shapes, and even multiply-connected shapes), since applications of mesoscopic superconductivity may well be not limited to simple perfectly-symmetric polygonal shapes.

For example, the so-called "2×2 antidot cluster", which is a superconducting microsquare containing four antidots (*i.e.* submicron holes), is now under renewed interest having a good perspective for flux quantum logic applications [27–29]. The experimental results have been compared with calculations in the London limit of the Ginzburg-Landau theory [27,28], the de Gennes-Alexander (dGA) model [28], and even the general GL theory for order parameter with variable magnitude [17]. While qualitative matches between the theories and experiment were claimed, a more detailed and quantitative analysis was called for at the same time [17]. Geurts *et al.* [30] solved temperature-dependent *nonlinear* GL equations for a thin film with four antidots and edge defects in a homogeneous magnetic field. They showed that V-AV states, which have never been observed experimentally, can be enforced by artificial fourfold pinning, with their local magnetic field enhanced by orders of magnitude.

In this paper, we do not consider antidots. Rather, we focus on the fundamental study of filled symmetric shapes beyond the few simple (mostly polygonal) shapes already studied so far such as triangles, squares, rectangles, and circles to examine in detail the phase boundary and the vortex configurations in the states generated just within the phase boundary. We believe this is a necessary first step, on account that we do not impose a mathematical symmetry *a priori* and thus our approach is completely general. As we shall see subsequently, symmetry arises in our numerical solutions spontaneously for the given physical condition. Thus our symmetric solutions originate from the physical symmetry of the sample. This way our method is not only an alternative but complementary approach to Chibotaru *et al.*'s. Note that in the actual example solutions presented below, we consider only symmetric geometries for the obvious reason that a totally irregular geometry would not allow us to have much insight on the correct solutions, unless there is a specific application.

Our computational approach has two distinct features. First, by using a FEM, we can readily treat complicated geometries. Regular polygons such as a pentagon are hardly more complicated mathematically than a square or triangle, but the analytical or even the numerical solution in domains of such shapes are not common. Our approach work very well for such geometries as well. In fact, in such cases, our solutions indeed conform to the correct symmetries of the samples, without the necessity to impose such conditions *a priori*. Second, the penalty method we use is a well-known technique for obtaining approximate solutions that satisfy some constraint(s) [in our case $\nabla \cdot \mathbf{A} = 0$ in the bulk and $\mathbf{A} \cdot \mathbf{n} = 0$ at surface(s)]. Our simulation results show that good results are obtained by applying such an approach, even though theoretically required group symmetry is satisfied only in an approximate sense.

We would like to point out another implication of this result. Since we aim to calculate the phase boundary for real physical samples, we believe our numerical method has

some merit for this purpose. In real situations, symmetry is broken in at least two ways. First, one has imperfections in the data; e.g., the sample surface invariably is slightly imperfect or even the applied field is not perfectly uniform. Second, thermal fluctuations can likely introduce random, and therefore nonsymmetric, perturbations into the system. Note also that in real situations there is likely one more symmetry-breaking disturbance from the electrical contact leads, which our FEM was shown to be able to handle appropriately [31]. In fact, this should be closer to the experimental situation presented by Chibotaru *et al.* Whether it means that symmetric vortex states may nucleate in a sample geometry and applied field with less than perfect symmetry is uncertain. Note that this "realistic" concern cannot be addressed in Chibotaru *et al.*'s model which consists of symmetric states only. In that case, the present scheme represents an important improvement, which allows direct implementation of geometric imperfection at any applied field. Note that the scheme also applies to the situation when a given distribution of pinning centers exist in the system or on its surface.

This article is organized as follows. In the next section, we present the LGL equations and a brief discussion of our numerical approach. In Section 3, we study nucleation for several previously-studied sample geometries, *i.e.*, squares, triangles, and disks, in order to establish our method. In Section 4, we study several geometries not studied before, *i.e.*, pentagon and four star shapes. Finally, Section 5 provides a summary of the results of this paper and some concluding remarks.

2 The mathematical and computational models

2.1 The linearized Ginzburg-Landau model

The general Ginzburg-Landau (GL) equation is given by [1]

$$\frac{1}{2m_s}\left(i\hbar\nabla+\frac{e_s}{c}\mathbf{A}\right)^2\psi+\alpha\psi+\beta|\psi|^2\psi=0, \tag{2.1}$$

where ψ is the complex-valued order parameter, with the superscript * denoting complex conjugation, $\mathbf{A}$ the magnetic vector potential, $\mathbf{b}=\nabla\times\mathbf{A}$ the total magnetic field [including the applied magnetic field ($\mathbf{H}$) and the induced magnetic field ($\mathbf{b}$ - $\mathbf{H}$)]. The supercurrent density is expressed as

$$\mathbf{j}_s=\nabla\times\nabla\times\mathbf{A}=\frac{e_s\hbar}{2im_s}(\psi^*\nabla\psi-\psi\nabla\psi^*)-\frac{e_s^2}{m_sc}|\psi|^2\mathbf{A}.$$

In the above, e_s is the "effective charge" of a Cooper pair which is twice the charge of an electron, and m_s its "effective mass" which can be selected arbitrarily, but the conventional choice is twice the mass of an electron. Also, c is the speed of light, and $\hbar=h/2\pi$, where h is Planck's constant.

For an isolated sample, the free boundary condition

$$\mathbf{n}\cdot\left(\frac{\hbar}{i}\nabla-\frac{e_s}{c}\mathbf{A}\right)\psi=0 \tag{2.2}$$

is satisfied; physically speaking, this condition implies that the normal component of the current at the boundary vanishes and the Neumann boundary condition on $|\psi|$ applies.

The phase boundary of a mesoscopic sample separating the superconducting state and the normal state in the field-temperature (H-T) space is an important measurable quantity to reveal the influence of the sample geometry. At this H-T phase boundary, the order parameter is vanishingly small and thus can be described by the *linearized* Ginzburg-Landau (LGL) equation [1]

$$\frac{1}{2m_s}\left(i\hbar\nabla+\frac{e_s}{c}\mathbf{A}\right)^2\psi=-\alpha\psi. \tag{2.3}$$

It is known that near the phase boundary, the induced magnetic field can be ignored so that the magnetic potential $\mathbf{A}$ in the Eqs. (2.2) and (2.3) corresponds to that for the external field, *i.e.*, $\mathbf{A}=\mathbf{A}_{ext}$, and the order parameter and magnetic field are decoupled [1]. Thus, if we have a gauge for the external magnetic field satisfying the boundary condition $\mathbf{A}\cdot\mathbf{n}=0$, the system above is *formally* identical with the Schrödinger equation with the Neumann boundary condition for an electron in a magnetic field. We use a penalty method [32, 33], to calculate the gauge $\mathbf{A}(\mathbf{x})$ satisfying the condition $\mathbf{A}\cdot\mathbf{n}=0$ along the sample boundary (and the condition $\nabla\cdot\mathbf{A}=0$ in the bulk).

Chibotaru et al. [23] provide an interesting comparison of their "vector potential gauge method" and numerical approach based on a finite difference method. Intuitively, it would seem better solutions can be obtained if one has a gauge function that satisfies the crucial $\mathbf{A}\cdot\mathbf{n}=0$ condition everywhere along the boundary rather than at a finite number of points on the boundary. In the finite element method, the desired gauge choice $\mathbf{A}\cdot\mathbf{n}=0$ on the boundary is enforced through a penalty method. As a result, the gauge for $\mathbf{A}(\mathbf{x})$ complying with the symmetry of the sample is reflected in the discretized equations to a greater extent than with finite difference methods, *i.e.*, our finite element methods enforces the gauge choice (weakly) along the whole boundary instead of just a boundary grid points. In order to obtain a solution to a desired accuracy, the approximation space may be increased in dimension, either through finer mesh (h-refinement), or by increasing the order of the polynomial basis (p-refinement), or both (h-p-refinement).

With the nonlinear term in the original Ginzburg-Landau equation ignored, the problem is *formally* the same as that of finding the quantized states of an electron in a magnetic field, which leads to the *Landau levels* in an infinite system. In particular, the lowest eigenvalue provides information about the phase boundary at which the nucleation of superconductivity occurs.

Let $\xi=(\hbar^2/2m_s|\alpha|)^{1/2}$ be the coherence length. Defining dimensionless variables as: $x\to x/\ell$ (where ℓ is an arbitrarily chosen length) and $\mathbf{A}\to\frac{\mathbf{A}}{\sqrt{2}H_c\ell}$, we then have, from Eqs.

(2.2) and (2.3), that

$$(i\nabla+K\mathbf{A})^2\psi=\eta\psi \tag{2.4}$$

and

$$\mathbf{n}\cdot(i\nabla+K\mathbf{A})\psi=0 \tag{2.5}$$

respectively, where

$$\eta=\frac{\ell^2}{\xi^2} \qquad \text{and} \qquad K=\frac{2\pi}{\Phi_0}\sqrt{2}H_c\ell^2=\frac{1}{\kappa}\left(\frac{\ell}{\xi}\right)^2. \tag{2.6}$$

The gauge-invariant phase gradient is given by $\nabla\varphi-K\mathbf{A}$ where $\psi=|\psi|e^{i\varphi}$ and φ is the phase of the order parameter.

In the following sections, ℓ is chosen to be the length of a side for a square and a triangle, the radius for a circle, and the distance from the center to a vertex for a pentagon. For stars, it is chosen as the distance from the center to an outer vertex, *i.e.*, the distance from the center to a vertex of the "circumscribing pentagon."

A weak formulation of Eqs. (2.4) and (2.5) is given by [25]:

$$\left(i\nabla\psi+K\mathbf{A}\psi,i\nabla\widetilde{\psi}+K\mathbf{A}\widetilde{\psi}\right)=\eta\left(\psi,\widetilde{\psi}\right), \quad \forall\,\widetilde{\psi}\in\mathcal{H}^1(\Omega), \tag{2.7}$$

where $\widetilde{\psi}$ is a test function belonging to the Sobolev space $\mathcal{H}^1(\Omega)$ that consists of complex-valued functions whose real and imaginary parts both have one square integrable derivative; we also use the inner product for complex-valued functions defined by

$$(\psi,\widetilde{\psi})=\int_\Omega(\psi\widetilde{\psi}^*+c.c.)d\Omega,$$

where *c.c.* denotes complex conjugation.

2.2 Discretization procedure

Standard Galerkin finite element discretizations of Eq. (2.7) lead to a generalized eigenvalue problems of the form

$$Ax=\eta Bx, \tag{2.8}$$

where

$$A=\begin{pmatrix}C & D\\ D^\top & C\end{pmatrix} \quad \text{and} \quad B=\begin{pmatrix}M & 0\\ 0 & M\end{pmatrix},$$

where $D^\top$ means the transpose of D.

For simplicity, we consider cylindrical samples (of any height) and constant applied magnetic fields H_{ext} that are parallel to the axis of the cylinder, *i.e.*, are perpendicular to

the cross-section of the sample. In this two-dimensional model, the entries of the matrices above are given by

$$C_{ij} = \int_\Omega \left(\frac{\partial \phi_i}{\partial x}\frac{\partial \phi_j}{\partial x} + \frac{\partial \phi_i}{\partial y}\frac{\partial \phi_j}{\partial y} + K^2 |\mathbf{A}|^2 \phi_i \phi_j \right) d\Omega,$$
$$D_{ij} = \int_\Omega K \left[\left(A_x \frac{\partial \phi_i}{\partial x} + A_y \frac{\partial \phi_i}{\partial y} \right) \phi_j - \left(A_x \frac{\partial \phi_j}{\partial x} + A_y \frac{\partial \phi_j}{\partial y} \right) \phi_i \right] d\Omega,$$

where A_x and A_y denote the components of $\mathbf{A}$, and

$$M_{ij} = \int_\Omega \phi_i \phi_j d\Omega \tag{2.9}$$

for $i,j = 1,\cdots,N$. In the above, Ω denotes the cross-section of the sample and $\{\phi_j\}_{j=1}^N$ denotes the finite element basis. Note that matrices A, B, C, and M are all symmetric and D skew-symmetric.

In all our examples, we use piecewise quadratic finite element basis corresponding to a triangulation of the sample domain [34]. Fig. 1 shows some examples of the triangulations used in our calculations. The left figure shows a uniform mesh consisting of a regular array of congruent triangles, while the right figure shows a conforming Delaunay triangulation created by the Triangle software package [35]. In most cases, we cannot use a uniform mesh so that we use a mesh similar to the one in the right figure. Fig. 1 also shows the nodal arrangement for quadratic finite element spaces, *i.e.*, there are nodes at the vertices and mid-sides of the triangles. The typical mesh we use to calculate the lowest eigenvalue consist of anywhere from 2,000 to 5,000 nodes. Refined mesh with about 10,000 nodes are used only to obtain vortex-antivortex states, where refinement is confined in the small region around the center of the sample where vortices and antivortices nucleate.

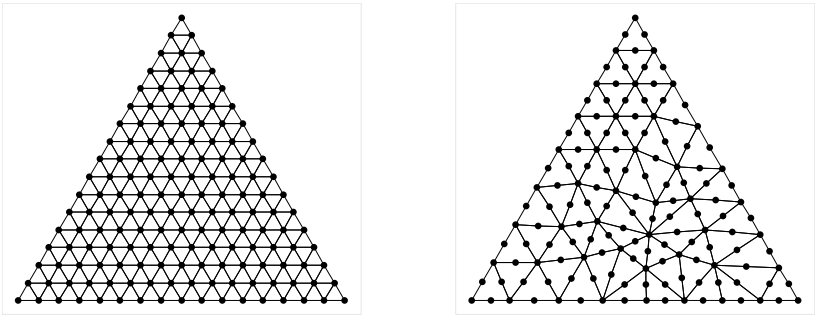

Figure 1: Examples of the triangulations used for calculations. Left: "regular" mesh created by a regular array of triangles in a triangular sample, Right: a Delaunay triangulation created by the software package "Triangle".

The desired gauge $\mathbf{A}(\mathbf{x})$ is calculated by a penalty method (see Section 2.3), then the discretized eigenvalue problem (2.8) is solved using the ARPACK software [36].

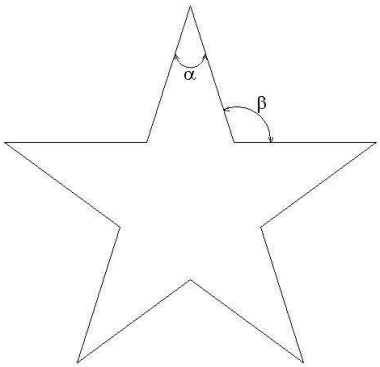

Figure 2: A star with a 36deg apex angle (*i.e.* α) — referred to as star-36 in this paper.

In the computational examples, $\ell = 2\mu m$ for the square, $2.28\mu m$ for the triangle, and $1\mu m$ for the disk and pentagon. We consider four cases of star-shaped samples having apex angles $\alpha =$ 90 degrees (star-90), 72 degrees (star-72), 36 degrees (star-36), and 18 degrees (star-18), which increasingly deviate from pentagon with the same area. (See Fig. 2.) For those stars, $\ell = 1.06$, 1.14, 1.46, and $1.91\mu m$ in turn, so that their areas are the same as that of the pentagon. Also, in Eq. (2.6), $H_c = 105Oe$ (aluminum) and $\Phi_0 = 2.07\times 10^{-7} G\cdot cm^2$.

2.3 Determination of the symmetry-preserving gauge by a penalty method

Since the magnetic potential we need to determine corresponds to that for the external magnetic field, the two-dimensional problem to be solved is given by

$$\frac{\partial A_y}{\partial x} - \frac{\partial A_x}{\partial y} = H_{ext}. \tag{2.10}$$

To fix the magnetic potential $\mathbf{A}$ satisfying Eq. (2.10), we apply the London gauge condition $\nabla\cdot\mathbf{A}=0$ in the cross-section Ω of the sample with the additional gauge choice $\mathbf{A}\cdot\mathbf{n}=0$ along the boundary Γ of Ω. These gauge choices may be viewed as constraints on possible solutions of Eq. (2.10); we choose to enforce these constraints using a penalty method. To this end, we define an objective function that consists of the magnetic energy plus two penalty terms:

$$\begin{aligned} F(\mathbf{A}) &= \int_\Omega \left[|\nabla\times\mathbf{A} - H_{ext}|^2 + s(\nabla\cdot\mathbf{A})^2 \right] d\Omega + c\int_{\partial\Omega} (\mathbf{A}\cdot\mathbf{n})^2 d\Gamma \\ &= \int_\Omega \left[\left(\frac{\partial A_y}{\partial x} - \frac{\partial A_x}{\partial y} - H_{ext} \right)^2 + s\left(\frac{\partial A_x}{\partial x} + \frac{\partial A_y}{\partial y} \right)^2 \right] d\Omega + c\int_{\partial\Omega} \left(A_x n_x + A_y n_y \right)^2 d\Gamma, \end{aligned}$$

where $s, c > 0$ are referred to as penalty parameters.

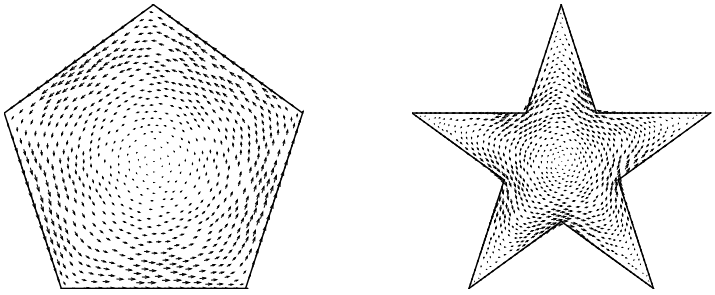

Figure 3: The vector potential for a pentagon, and a star obtained by a penalty method.

We express the components of the vector potential in terms of the finite element basis $\{\phi_j\}_{j=1}^N$, *i.e.*,

$$A_x^h = \sum_{j=1}^N e_j \phi_j \qquad \text{and} \qquad A_y^h = \sum_{j=1}^N f_j \phi_j.$$

We substitute these expression in the above expression for $F(\mathbf{A})$ and then determine the coefficients e_j and f_j by minimizing the resulting discretized functional with respect to those coefficients, *i.e.*, by solving the equations

$$\frac{\delta F}{\delta e_j} = 0 \qquad \text{and} \qquad \frac{\delta F}{\delta f_j} = 0$$

for $j = 1, \cdots, N$. The solution obtained in this manner is an approximate solution of Eq. (2.10) along with the gauge choices we have made. See Fig. 3 for illustrations of such approximations in a pentagon and a star. It is important to note that our procedure is general, *i.e.*, it can be used to determine **A** satisfying Eq. (2.10) and the gauge choices for *arbitrarily shaped sample cross sections* Ω.

3 Nucleation in mesoscopic finite-cylinder samples with previously-studied shapes

In Fig. 4 the phase diagrams obtained for mesoscopic finite-cylinder samples with square-, triangle-, and disk-shaped cross sections are gathered. These previously-studied shapes are studied here mainly for the purpose of establishing our method. For comparison, the phase diagram for a pentagonal cross section (to be studied in Section 4) is also included. Each curve in Fig. 4 presents the lowest eigenvalues of various irreps for a mesoscopic finite-cylinder sample with circular (solid curve), pentagonal (dotted), square (dashed), or triangular (dot-dashed) cross section for varying magnetic flux. The flux is defined as $\Phi = H_{ext} S$, where H_{ext} is the applied magnetic field, and S, the area of whatever shape

under study. Thus, we present the eigenvalues in terms of

$$\frac{S}{\xi^2}=\frac{\ell^2}{\xi^2}\cdot\frac{S}{\ell^2},$$

where the nondimensional sample size S/ℓ^2 is determined from the geometry. This way, eigenvalues for samples of different shapes can be plotted together and rationally compared. Note that $\Phi/\Phi_0 \propto H_{ext}$ and $S/\xi^2 \propto [1-T_c(H_{ext})/T_c(0)]$. So the critical temperature $T_c(H_{ext})$ decreases as S/ξ^2 increases.

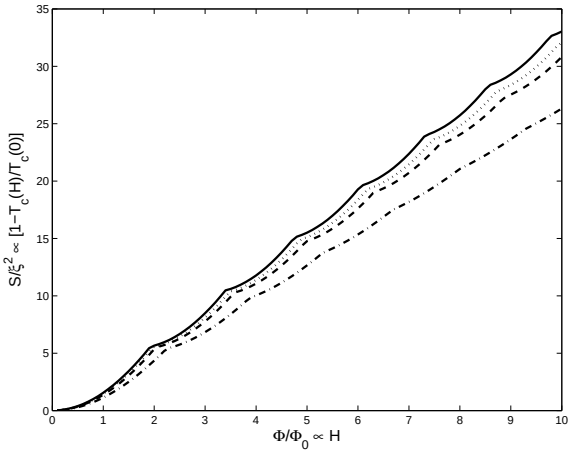

Figure 4: H-T phase boundary for all convex samples considered. Solid curve corresponds to the circular cross section, dotted curve to the pentagon, dashed curve to the square, and dot-dashed curve to the triangle.

From Fig. 4, we can see that S/ξ^2 has a generally linearly upward trend as Φ/Φ_0 increases, but with an oscillatory behavior superposed on it. This oscillatory behavior with slope discontinuities — the cusps — occurring at a discrete set of flux values arises from the change of the winding (or vorticity) quantum number L in the eigenvalues plotted. Note that the phase boundary plotted in Fig. 4 matches the phase boundary identified as the lowest envelope of the N curves of the lowest eigenvalues of N irreps reported in a previous work [23]. ($N=4$ for a square, and 3 for an equilateral triangle.) Also, in the intervals between the subsequent cusps of each curve in Fig. 4, the total winding number remains constant. Moreover, the winding number always increases by one as each cusp is crossed as the total magnetic flux Φ in the sample is increased. All curves exhibit similar oscillatory behavior in S/ξ^2 as the input magnetic flux is changed, but have different locations of the transition points. The transition points between different vortex configurations in each sample are summarized in Table 1. Again, the transition points between different vortex configurations in a pentagon are included for comparison purposes.

It is observed that as the number of sides of a polygon increases, *i.e.*, as $N\to\infty$ for a C_N symmetry, so that the sample shape approaches a disk, the phase-boundary curve shifts upward and the transition points shift to the left, resulting sometimes in higher-L Landau levels for a given magnetic flux. If these samples have an identical coherence

Table 1: Calculated transition positions in the phase boundary curves at which a change of winding number of the system occurs for finite-cylinder samples with different cross-sectional shapes and any height.

$L \to L+1$	Circle	Pentagon	Square	Triangle
$0 \to 1$	2.0	2.0	2.1	2.3
$1 \to 2$	3.4	3.5	3.6	3.9
$2 \to 3$	4.8	4.9	5.0	5.4
$3 \to 4$	6.1	6.2	6.4	6.7
$4 \to 5$	7.4	7.5	7.7	8.1
$5 \to 6$	8.6	8.8	8.9	9.4

length $\xi(0)$ (the Ginzburg-Landau coherence length extrapolated to $T=0$), their phase-boundary curves can be compared. In this case, it can be said that, for the same area subject to decreasing magnetic field H, the superconductivity nucleates in the order of triangle, square, pentagon, then disk (*i.e.* increasing N). (This is because nucleation of superconductivity is easier at acute corners of the sample.) All these behaviors closely match previously reported results [23] both qualitatively and quantitatively, except those for a pentagon, which to our knowledge have not been obtained before. The oscillatory behavior of $1/\xi^2$ (hence the depression of T_c from simple linear behavior) is similar to that observed in a disk [13, 14].

Figs. 5 (a) to (d) show the vortex configuration nucleated at $\Phi/\Phi_0 = 5.5$ in a square sample. Fig. 5 (a) shows the magnitude of the order parameter, Fig. 5 (b) the gauge-invariant phase gradient, and Fig. 5 (c), (d) the phase of the order parameter. A very small region near the center is zoomed in all the figures, except Fig. 5 (c). The phase of the order parameter changes from 0 (blue) to $\pm 2\pi$ (red) as a closed curve around the core of a vortex/antivortex is traced in the counterclockwise direction. The same color scale was used from the minimum (blue) to maximum (red) levels in the magnitude of the order parameter. Note that blue appears dark gray and red appears light gray in grayscale print.

In the weak superconductivity just nucleated across the phase boundary, vortices and antivortices are difficult to identify because they are tiny and located in close proximity of each other. Thus, plotting the magnitude of the order parameter is not convenient for this purpose. Also, the gauge-invariant phase-gradient plot gets messy quickly as the vortex cores are approached due to the rapid variation of the phase there. This trend becomes even worse as we examine nonrectangular samples. Since vortices are topological excitations, the phase variation around a vortex is discernable even far from the vortex core. Also the origin around which the phase spans gives precise information of the location of vortex cores.

The magnitude and the gauge-invariant phase gradient of the order parameter must have the symmetry of the sample, being associated with the non-degenerate ground state solution of a linear eigenvalue problem, but the phase of the order parameter does not have to have this symmetry, even in the gauge where the vector potential does have this symmetry. This is because when the discrete rotation operator of the symmetry operation

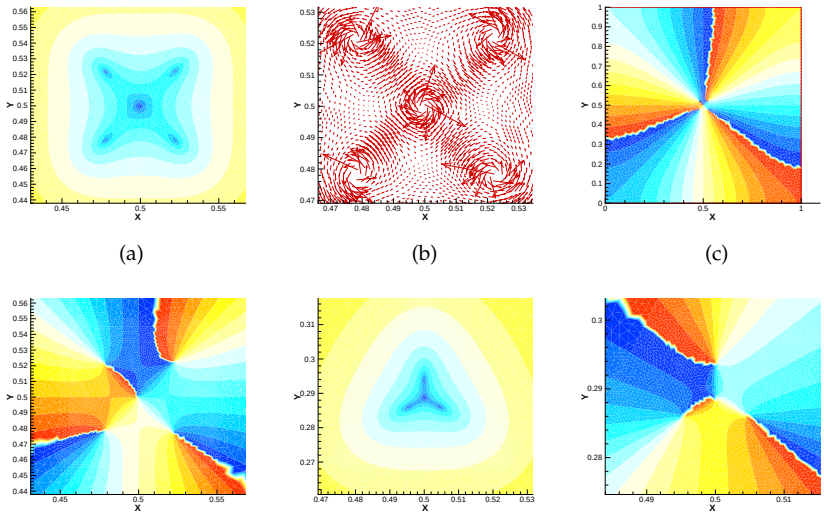

(a) (b) (c)

(d) (e) (f)

Figure 5: (Color online) Plots corresponding to the superconducting state nucleated in a square sample in an applied magnetic flux $\Phi=5.5\Phi_0$ (a-d) and in a triangular sample in an applied magnetic flux $\Phi=4.5\Phi_0$ (e, f). All plots except (c) are zoomed in to show four vortices and an antivortex in a small region around the center. (a), (e) Order parameter; (b) gauge-invariant phase gradient; (c), (d) and (f) phase.

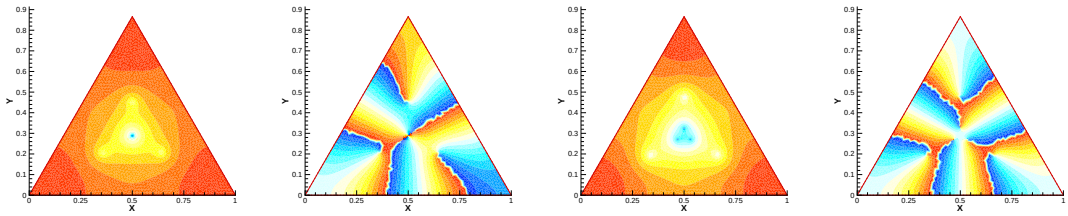

(a) (b) (c) (d)

Figure 6: (Color online) Plots corresponding to the superconducting state nucleated in a triangular sample in an applied magnetic flux $\Phi=8.7\Phi_0$ (a,b) and $\Phi=10.0\Phi_0$ (c,d). (a), (c) Order parameter, (b), (d) phase.

is applied to the wave function, it needs only regenerate the wave function times some constant phase factor, rather than the wave function itself.

The coexistence of vortices and antivortices forces us to examine the phase very carefully to find the exact vortex state. In Fig. 5 (c) it appears that the square carries only three vortices since it appears to have three contiguous intervals of phase variation $[0,2\pi]$. But zooming into the region around the center in Fig. 5 (d) reveals four vortices and an antivortex at the center: around each of the four vortices located along the diagonals, the phase increases from 0 (blue) to 2π (red) in the *counterclockwise* direction. Around the center, the phase increases from 0 (blue) to 2π (red) in the *clockwise* direction to show that there is an antivortex there.

Figs. 5 (e) and (f) shows the vortex configuration nucleated at $\Phi/\Phi_0=4.5$ in a trian-

gular sample. The plots of order parameter and phase clearly show three vortices and an antivortex. From Fig. 4 one can see that the winding number $L=2$ for $\Phi=4.5$ which an examination of Fig. 5 (f) confirms since it shows that there are three vortices and one antivortex.

Note that these V-AV states in Fig. 5 were already found in [19–23]. However, it is important that whereas [19–23] has imposed symmetry in their solutions, in our results symmetry was not imposed but appeared spontaneously. This shows that our method can allow us to discover any accidental symmetry which might exist in the solutions, which cannot be seen *a priori*. (Note that aside from numerical errors, our solutions are actually "exact solutions", in the sense that we did not make any intentional approximations.)

Figs. 6 (a) and (b) show the vortex configuration for $\Phi/\Phi_0=8.7$ and Figs. 6 (c) and (d) do likewise for $\Phi/\Phi_0=10.0$ both for the same triangular sample in Figs. 5 (e) and (f). For $\Phi/\Phi_0=8.7$, the vortex state consists of three singly quantized vortices toward the corners and a doubly quantized vortex at the center. We will call it the "3+2" state. The vortex state for $\Phi/\Phi_0=10.0$ carries six singly quantized vortices, all aligned along the lines connecting the center point to the three vertices. We will call it the "3+3" state. Note that these vortex states occur near the phase boundary; the nucleation fields are calculated to be $H_{c3}=2.399H_{c2}$ for the vortex state in Figs. 6 (a) and (b), and $H_{c3}=2.387H_{c2}$ for that in Figs. 6 (c) and (d). These values are obtained from the simple relation

$$\Phi/\Phi_0=(H_{c3}/H_{c2})(S/2\pi\xi^2).$$

Using this relation one can easily convert Fig. 4 to a plot of H_{c3}/H_{c2} vs. S/ξ^2. To change it to a plot of H_{c3}/H_{c2} vs. $(1-T/T_c)$, one needs as input the value of $S/\xi(0)^2$.

For a superconducting disk, a giant vortex state is the ground state solution, whose orbital angular momentum L is also the total winding number. However, in square or triangular samples the vortex configuration in the ground state might be different due to the finite order of their group symmetry. It was proposed that the total winding number in a triangular sample can be written as $L=n+3m$ for small L's, where $n=0,1,-1$ is the vorticity number of the vortex located at the center and $m=0,1,\cdots$ is the number of vortex triads oriented parallel to the sample [20,21,23]. In other words, the winding number of the vortex at the center of a triangle can take the values 0, 1, or -1 only. However, for a higher winding number $L=5$ Figs. 6 (a) and (b) show a doubly-quantized vortex (with $L=2$) at the center and three vortices outside (the "3+2" state)[‡]. Note that the above rule

[‡]In fact, very close the center, the solution shows unphysical symmetry breaking with the center doubly-quantized vortex ($L=2$) splitting into two very closely spaced $L=1$ vortices, but it is an artifact due to the fact that the random triangulation of the sample weakly broke the symmetry of the sample, and the very weak magnitude of the order parameter near the sample center made its phase very sensitive to weak perturbations. Since the two vortices juxtaposed around the center in the square are located very closely to each other so as to almost overlap, we believe that if perfect symmetry is imposed on the vector potential $\mathbf{A}(\mathbf{x})$ and the triangulation it would render these closely spaced vortices into a multiply-quantized vortex. The same trend applies to all other geometries.

$L=n+3m$ would predict six vortices surrounding an antivortex at the center for $L=5$ (the "6-1" state). [Chibotaru *et al.* might have considered $n=-1$ the same as $n=2$, because they belong to the same irrep of the C_3 group, but these two values of n actually give two different (anti- and giant) vortices at the center of the sample, and should not be identified. Another possibility is that Chibotaru *et al.* might have concluded that $n=-1$ is always energetically more favorable than $n=2$, but we find that for some L the opposite is true, and we have given a possible reason below.]

From our experience, we do not think there is a degeneracy in the ground state, although at the present time we do not yet know how to check this possibility carefully. We at least do not find their state (six vortices surrounding an antivortex) as the next higher state in our calculations. Our next higher state always turns out to be a state with a value of L one higher, and it is clearly not degenerate with the ground state we find.

Near the phase boundary, where the LGL equation is valid, the superconducting wave function is highly non-uniform: It is large near the sample boundary only, and diminishes in a length scale of the GL coherence length as the inside of the sample is approached. Thus the closer is a vortex to the sample boundary, the larger should be the free-energy cost to form the vortex core. In this sense vortices should like to form deep inside the sample, and avoid the sample boundary. We shall call this effect on the vortices "surface repulsion effect", but emphasize that it is not the same as the "surface-barrier effect" that is obtained by studying the non-linear Ginzburg-Landau equations. From this point of view, we believe that the vortex state we have found (viz., the "3+2" state) should have a lower free energy than the "6-1" state discussed in [20, 21, 23].

The surface-repulsion-effect argument does not seem to apply cleanly to the vortex state we found for $\Phi/\Phi_0=10.0$ in Figs. 6 (c) and (d) (viz., the "3+3" state) to justify that it is more stable than the state implied by a sketch in Fig. 11 of [23], where 6 vortices form a single triangle, with three vortices at the vertices of this triangle, and the other three at the midsides. We simply did not find this sketched configuration in our calculation. Perhaps the sketches provided in that figure for $L=5,6$ are merely intuitive guesses on how the vortex structures at those values of L might be. [Actually the "3+3" state we found is consistent with their $n+3m$ rule, with $n=0$ and $m=2$, whereas their $L=6$ state is not.]

The evidence of "surface repulsion effect" is yet reinforced by Fig. 7 showing a triply-quantized vortex (with $L=3$) at the center and four vortices outside in a square sample. The total winding number is $L=7$ and we shall call it the "4+3" state. It was also proposed in [20,21,23] that the total winding number in a square sample can be written as $L=n+4m$ for small L's, where $n=0,1,2,-1$ is the vorticity number of the vortex located at the center and $m=0,1$. Thus this rule of theirs applies to $L\leq 6$ only, and really does not apply to $L=7$. Still, our result for $L=7$, where an $L=3$ giant vortex is found at the center of the sample, shows explicitly that their rule can not be applied beyond $L=6$. [Again Chibotaru et al. might have considered $n=-1$ the same as $n=3$, because they belong to the same irrep of the C_4 group, but these two values of n actually do not give the same (anti- or giant) vortex at the center, and should not be identified.]

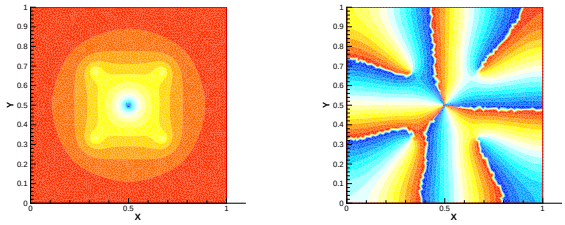

(a) (b)

Figure 7: (Color online) Plots corresponding to the superconducting state nucleated in a square sample in an applied magnetic flux $\Phi = 11.0\Phi_0$. (a) Order parameter, (b) phase.

Mel'nikov *et al.* [37] have used defects of increasing sizes to examine the stability of maximally symmetric vortex configurations obtained near the phase boundary, such as one with four vortices on the diagonals and one antivortex at the center of a square sample, forming a centered square pattern, thus having the same symmetry as that of the sample. They found that the antivortex would annihilate one of the vortices if the size of the defect was increased to $0.16\xi \times 0.08\xi$. They thus concluded that such a maximally symmetric state was very sensitive to a small perturbation to the symmetry of the sample geometry that might be caused by defects or fluctuations. Our V-AV states show that our method can reflect the sample symmetry very accurately. Mel'nikov *et al.* also introduced a small defect (normal metal) on the sample boundary to perturb the fourfold symmetry of their numerical scheme (explicit Euler) leaving the order parameter and current distribution almost undisturbed. This way they could obtain the branches on the magnetization curve with an odd total vorticity (including their "4+3" state at $H = 1.26H_{c2}$), whereas the even-vorticity branches could already be found by them without introducing the defect. The fact that we did not have to use any artificial defect to obtain the "3+2" and "4+3" symmetric states (spontaneously) gives a rather firm footing to our method.

When studying the non-linear Ginzburg-Landau equations deep inside the phase boundary of a mesoscopic sample [31], we find that as the size of the sample becomes smaller and smaller, the interaction between vortices and sample surfaces and shape becomes more and more important. The influence of the sample surfaces and shape on the superconductivity is especially strong on the phase boundary. For example, in the above-mentioned three vortex states we obtained here by solving the LGL equation (*i.e.*, the "3+2", "3+3" and "4+3" states), the system appears to choose vortex configurations satisfying the required group symmetry and possibly also taking into account of the surface repulsion effect. (There are likely other mechanisms in determining the vortex configurations that we are not aware of.)

In the study of the non-linear Ginzburg-Landau equations, it was found that $L(>1)$ singly quantized vortices are preferred energetically than a single giant vortex of vorticity quantum number L since the kinetic energy of a vortex is proportional to the square of its vorticity [38]. However, this is evidently not the case near the nucleation critical field, where the highly non-uniform superconducting order parameter ψ can favor a giant

vortex sitting at the center of the sample where ψ is the weakest, than several singly quantized vortices which must be distributed closer to the sample boundary, where ψ is larger.

In a previous study [18], an asymptotic formulas for the phase boundary were derived. The leading order terms in the expansions can be written as

$$\frac{S}{\xi^2} \sim 2\pi\mu_c \frac{\Phi}{\Phi_0} \qquad \text{for } \Phi/\Phi_0 \ll 1$$

and

$$\frac{S}{\xi^2} \sim 2\pi\zeta_0 \left(\frac{\Phi}{\Phi_0}\right)^2 \qquad \text{for } \Phi/\Phi_0 \gg 1.$$

The coefficients are given by $\mu_c = 0.55$ and 0.59 for the square and circular cross sections, respectively and the corresponding values of ζ_0 are 0.22 and 0.25, respectively. Thus, the phase boundary curve is parabolic for small fluxes and linear for large fluxes.

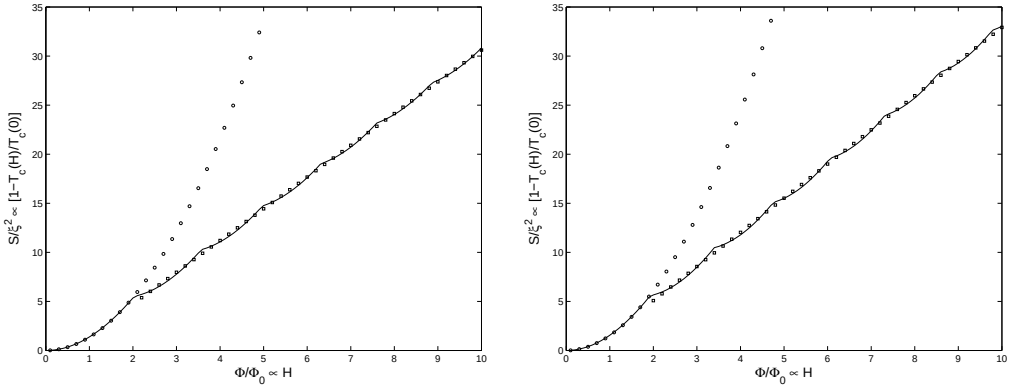

Figure 8: Curve fits for the H-T phase boundaries (solid curves) for mesoscopic finite-cylinder samples with square (left) and circular (right) cross sections. Circles (○) show the parabolic fits; squares (□) show the linear fits.

In Fig. 8, we present the phase diagrams for square and circular cross sections. We also display parabolic fits ($y = ax^2$) for the $L = 0$ portions of each curve and linear fits for the rest of the phase diagrams ($L \geq 1$). For the square cross section, we obtain the values $2\pi\mu_c = 3.23$ from the linear fit and $2\pi\zeta_0 = 1.35$ from the parabolic fit. Note that in the previous study [18], the values $2\pi\mu_c = 3.46$ and $2\pi\zeta_0 = 1.38$ were obtained. For the circular cross section, we obtain $2\pi\mu_c = 3.48$ from the linear fit and $2\pi\zeta_0 = 1.52$ from the parabolic fit, while the previous study obtained $2\pi\mu_c = 3.71$ and $2\pi\zeta_0 = 1.57$.

4 Nucleation in mesoscopic finite-cylinder samples with cross-sectional shapes not studied previously

The method used in previous studies [20, 21, 23] is effective for relatively simple geometries, but becomes difficult to apply when the sample geometry becomes more complex,

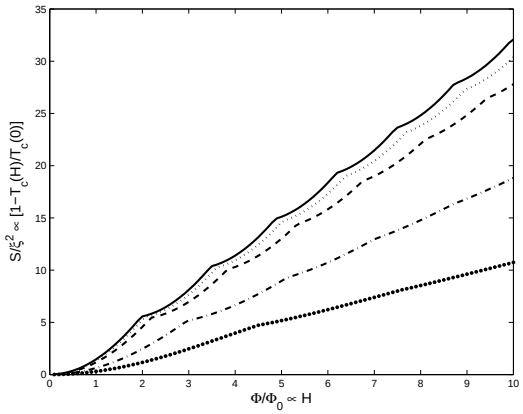

Figure 9: H-T phase boundaries for pentagonal cross section (solid curve) and for four star-shaped cross sections, with light dotted curve corresponding to the star-90 case, dashed curve to star-72, dash-dot to star-36, and heavy dotted curve to star-18. (The numbers refer to the apex angles of the stars, and all shapes have the same area.)

such as pentagonal or a star-shaped. The primary reason for the development of our finite-element-based method is so that samples having more complex geometries can be treated with relative ease. We illustrate this point by considering simulations for pentagonal and star-shaped cross sections.

Dikin *et al.* [39] studied phase transitions in a four-pointed star-shaped sample by measurement and numerical calculation. By solving full nonlinear Ginzburg-Landau equations using a self-consistent method [15, 16] near the critical temperature, strong inhomogeneity of the order parameter was obtained. T-H phase diagrams at various R/R_N, were measured and compared with the calculational results, which took into account this inhomogeneity. The presence of magnetic vortices was hinted by the oscillations in the measured critical temperature $T_c(H)$, a subject we have illuminated more in our paper.

Fig. 9 presents the lowest eigenvalues for four mesoscopic finite-cylinder samples with star-shaped cross sections of different apex angles α, all having the same area as the pentagon also plotted together, as the applied magnetic flux increases. Note that for the

Table 2: Calculated transition positions in the phase boundary curves at which a change of winding number of the system occurs for samples with different cross-sectional shapes.

$L \to L+1$	Pentagon	Star-90	Star-72	Star-36	Star-18
$0 \to 1$	2.0	2.1	2.2	3.0	4.5
$1 \to 2$	3.5	3.7	3.9	5.2	7.7
$2 \to 3$	4.9	5.1	5.4	7.1	
$3 \to 4$	6.2	6.4	6.8	8.8	
$4 \to 5$	7.5	7.7	8.2		
$5 \to 6$	8.8	9.0	9.5		

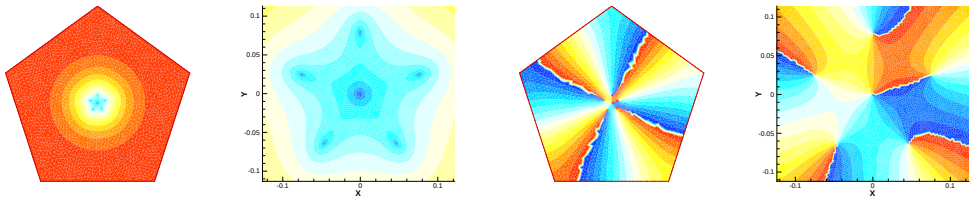

(a) (b) (c) (d)

Figure 10: (Color online) Plots corresponding to the superconducting state nucleated in a pentagon in an applied magnetic flux $\Phi=6.8\Phi_0$ showing five vortices and an antivortex in a small region around the center. (a,b) Order parameter, with a zoomed-in view on the right. (c,d) Phase plot, with a zoomed-in view on the right.

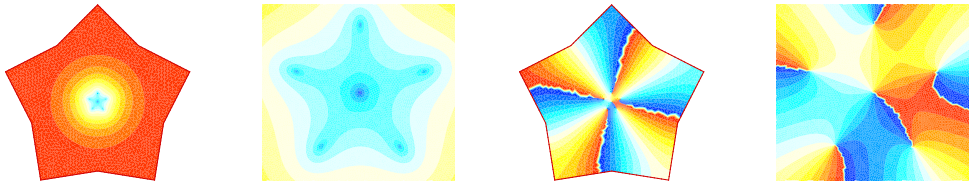

(a) star-90

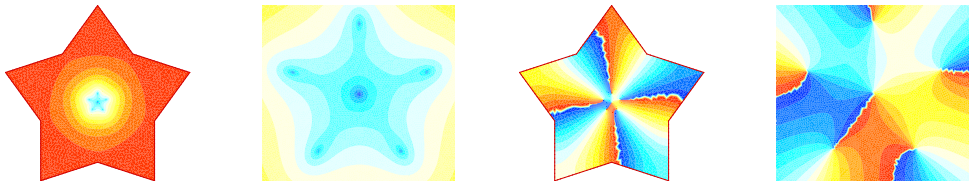

(b) star-72

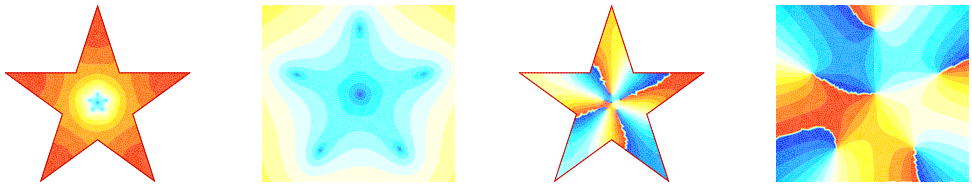

(c) star-36

Figure 11: (Color online) Plots corresponding to the superconducting state nucleated in (a) the star-90 in an applied magnetic flux $\Phi=7.0\Phi_0$, (b) the star-72 in $\Phi=7.5\Phi_0$, and the star-36 in $\Phi=9.4\Phi_0$. All plots show five vortices and an antivortex in small region around the center. In each figure of (a) to (c), top row shows the order parameter, zoomed on the right, and bottom row shows phase plot, also zoomed on the right.

concave surfaces in the stars the angle is given as $\beta=72+\alpha$ degrees. (See Fig. 2.) Thus as α decreases, the concave vertices become more pointed at the same time. The general behavior is similar to those of the samples in the previous section. The transition points between different vortex configurations in each sample are summarized in Table 2.

Fig. 10 presents the V-AV configuration in a pentagon. For samples with (5-pointed) star-shaped cross section, we define a deviation parameter $\epsilon = (R_1 - R_2)/R_{av}$, where R_1 is the radius of the outer circumcircle, R_2 that of the inner circumcircle, and R_{av} is the hydraulic radius of the sample, which is defined by $S = \pi R_{av}^2$. Note that as concavity increases, $R_2 \to 0$, $R_1 \to \infty$, and $\epsilon \to \infty$.

Fig. 11 presents the V-AV configurations captured in each sample. These correspond to $\epsilon = 0.347$ (star-90), 0.502 (star-72), 1.034 (star-36), and 1.712 (star-18).

As the apex angle α of a star is reduced (or its deviation parameter ϵ is increased) at constant area, nucleation of superconductivity becomes increasingly concentrated near the convex vertices. Thus the phase boundary becomes increasingly determined by the apex angle of the star. However, the residual weak Little-Park-like oscillations that still exist on the phase boundary curves containing weak cusps reveal that the discrete changes of the winding quantum number L always still play a role (but smaller role for smaller α). It means that everywhere along the boundary of the star of any α and ϵ the order parameter is always non-vanishing, allowing the quantum number L to be always well-defined. But the order parameter becomes ever weaker near the sharper concave vertices of a star of smaller α (or larger ϵ), which explains why this L quantization plays an ever weaker role in determining the phase boundary as α decreases.

Still, the sample always has a well-defined V-AV configuration at any α and ϵ and H. The L-transition points are delayed to larger H or Φ/Φ_0 for smaller α and larger ϵ, likely because the vortices must now exist closer to the boundary.

Examining the phase boundary curves for these nonconvex star-shaped cross-sections, it is evident that nucleation occurs at a higher H for a given T, or at a higher T for a given H, for a star of smaller α (or larger ϵ), *i.e.*, for larger concavity. This is simply because near a convex vertex of the star of a smaller α the vector potential variation becomes smaller, leaving mainly only a constant vector potential there which can be transformed away by a local gauge transformation, and therefore can not affect the nucleation phase boundary of the sample [which means that the $T_c(H)$ becomes closer to $T_c(0)$].

The star-shaped samples show a marked drop in S/ξ^2 while displaying vortex configurations that fit the sample geometry. These star shapes have C_5 symmetry as for a pentagon, as is demonstrated by the vortex configuration in the figures.

To understand the behavior of stars better, we consider the studies of wedge-shaped superconductors. It is known that superconductivity is enhanced at sample corners with angle $\alpha < \pi$ [40–44]. It was shown that H_{c3}/H_{c2} approaches infinity as $\alpha \to 0$, while H_{c3}/H_{c2} approaches 1.695 as $\alpha \to \pi$ (flat surface). However, not much is found in the literature about concave surfaces ($\alpha > \pi$). In one of the previous studies [40], a variational calculation was presented for a corner with $\alpha = 1.5\pi$ and it was shown that the order parameter is weakest at the concave corner (*i.e.*, it decays the most rapidly in the direction into the sample at the concave corner.) In the following work [41] by the same trial function used for the $\alpha = 1.5\pi$ corner, the nucleation field was estimated as $H_{c3}/H_{c2} = 1.6589$, independent of α. This is easy to understand since nucleation of superconductivity will avoid concave corners, and will seek convex corners, where the nucleation critical field is

higher. For an infinite wedge with $\alpha > \pi$, there are no convex corners, so nucleation will be mainly at the edge away from the concave corner. This should give $H_{c3}/H_{c2} = 1.695$ independent of α as long as α is $\geq \pi$. Dikin *et al.* [39] obtained 1.6589 instead of 1.695 because its variational approach can only give a lower bound to this number.

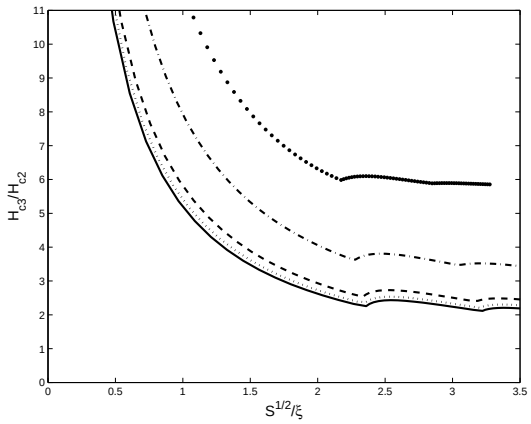

Figure 12: H-T phase boundary for various cross sections not studied previously: pentagon (solid curve), star-90 (light dotted curve), star-72 (dashed curve), star-36 (dash-dot), and star-18 (heavy dotted curve).

Fig. 12 presents H_{c3}/H_{c2} vs. $S^{1/2}/\xi$ curves for pentagon and star-90 to star-18. The nucleation field H_{c3}/H_{c2} is larger as one moves from a pentagon to star-18 for a given $S^{1/2}/\xi$ value. That is, as α is reduced, or ϵ is increased. The H_{c3}/H_{c2} value at the highest plotted value of $S^{1/2}/\xi$ for each curve (corresponding to $\Phi/\Phi_0 = 10$ in each simulation) is 2.068 (star-90), 2.260 (star-72), 3.338 (star-36), and 5.854 (star-18), respectively. Since these values show very little change as $S^{1/2}/\xi$ further increases, we believe these values of H_{c3}/H_{c2} are close to the asymptotic limit as $S^{1/2}/\xi \to \infty$. These values should correspond to the H_{c3}/H_{c2} values of infinite wedges with the corresponding apex angles. The fitting formula of Schweigert and Peeters for wedges [43] produces 1.972, 2.170, 3.275, and 5.799, respectively for the same vertex angles. Therefore, for large $S^{1/2}/\xi$, the phase boundary is decided by the vertex angle only, and is independent of the precise shape and the symmetry of the sample. But the vortex structure nucleated inside the sample is still decided by the precise shape and symmetry of the whole sample. (See Fig. 11.)

As another consequence of our observation above, we expect H_{c3}/H_{c2} of star-90 and that of a square to be very close at very large $S^{1/2}/\xi$, but we also find it very interesting that they differ by only 1.82% even at $S^{1/2}/\xi = 2$, and for $S^{1/2}/\xi = 0.1$, their difference increases to 2.05%. (Note that the difference of H_{c3}/H_{c2} between a pentagon and star-90 in the same range of $S^{1/2}/\xi$ is above 8%.) In the same context, we expect H_{c3}/H_{c2} of star-72 and that of a triangle ($\alpha = 60$ deg) are close since their apex angles are close. In our calculation, their differences are within 6.2% in the range of $S^{1/2}/\xi$ tried. Fig. 13 presents H_{c3}/H_{c2} vs. $S^{1/2}/\xi$ curves for a square and star-90, and a triangle and star-72. Note the close match between star-90 (dotted curve) vs. square (+). Also the nucleation field curve for triangle (o) is close to that for star-72 (dashed curve).

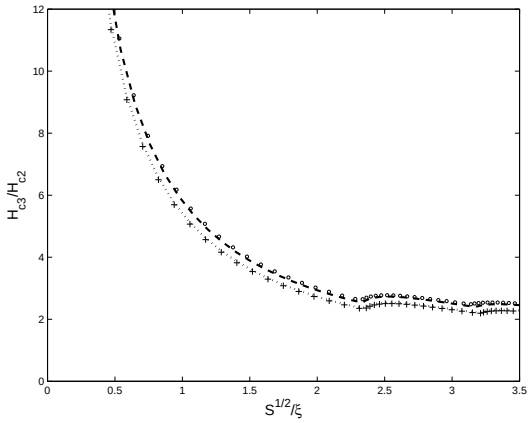

Figure 13: Comparing H-T phase boundary for various cross sections: star-90 (dotted curve) vs. square (+) and star-72 (dashed curve) vs. triangle (o).

In another point of view, the stars behave as a pentagon with a smaller effective area. Our results shows that nonconvexity decreases the effective area so that the measured level S/ξ^2 would decrease. However, as long as the nonconvex sample maintains the same C_N symmetry as the convex sample, it follows the same L-transition rule as the convex sample, only with an effective area smaller than that of the convex sample. In other words, even though the sample area is a little off, we can still obtain the same V-AV configurations as long as the symmetry of the sample shape is right. For high temperature superconductors, it has been shown that it is possible to fabricate epitaxial films with desired symmetry [45]. Although the fabricated hexagonal films are not yet mesoscopic in size, we believe that mesoscopic films of highly symmetric shapes can be made within the current technologies.

5 Summary and conclusions

We have determined the T-H phase boundary for various sample geometries using a penalty finite element method. This method is developed here mainly to handle more complex shapes of mesoscopic samples. The triangle, square and disk shapes are studied here first in order to establish our method. It is then applied to pentagon and four star shapes of different apex angles in order to demonstrate the flexibility and versatility of our method. We also found vortex-antivortex configurations for each sample that accurately reflect the discrete symmetry of each sample boundary. The transition points between different vortex configurations in each sample are summarized in Tables 1 and 2. Note the good match of those transition points in the triangle, square and disk samples with those in previous study [23] except that in our approach the symmetry in the solutions is obtained rather than imposed. This part of the study confirms the accuracy of the present approach.

For higher L's, our approach predicts a GV surrounded by singly-quantized vortices both in a triangle and a square, while satisfying the group symmetry perfectly, in contrast to the V-AV states that previous studies [20, 21, 23] predict for the same values of L.

The behavior of the pentagon was very consistent with those of square and triangles, and this is a somewhat expected result. However, it was never really studied in previous works, so we examined and verified the result in the framework of a new numerical approach. Furthermore, the stars were found to behave closely to pentagon in their vortex configurations, while their nucleation fields H_{c3}/H_{c2} approach those of infinite superconducting wedges of the same apex angles for large $S^{1/2}/\xi$. But even for moderate $S^{1/2}/\xi$ their differences are found to be small, especially for stars of small apex angles.

It should be noted that in our current study the L-quantum vortices and antivortices at the center of the sample are actually found to be L singly quantized vortices or antivortices in very close proximity, in an arrangement which breaks the sample symmetry. So, for example, the $L=2$ case consists of two very closely located but separate vortices. As another example, the $L=6$ case in a square consists of 4 vortices located along the diagonals plus two vortices juxtaposed in very close proximity around the center. That is, if a very small center region is blown up, a loss of the square symmetry with the center doubly-quantized vortex ($L=2$) actually appearing as two $L=1$ vortices in very close proximity is found, the reason of which has already been explained. But it is mainly because the symmetry of the problem is lost in such fine scales in our approach. This undesirable result reflects the limit of accuracy of our approach.

However, the fact that vortex-antivortex configurations were captured in all different samples shows that our approach can effectively produce symmetry-conserving solutions in samples of various geometry. The fact that multiply-quantized vortices were not found suggests that the given symmetry should be satisfied locally, in a finer scale than that for vortex-antivortex states. Our current approach used a quadratic penalty method. More advanced algorithms such as ℓ_1 penalty method or augmented Lagrangian method are available [46]. For the sake of computational efficiency, unstructured, nonuniform triangulations (determined using the Triangle [35] software) have been used to create very fine meshes in the area around the center to obtain vortex-antivortex configurations. It is also possible to construct a regular Delaunay triangulation with refinement in a desired area. Also, ever-advancing computer capacity holds the promise that better solutions can be obtained.

Our method gives a good vantage point for studying the T-H phase boundaries and vortex configurations for samples with arbitrary shapes, including multiply-connected shapes such as mesoscopic samples with randomly- or strategically-placed holes. Optimal values of the penalty parameters can be found by tuning the algorithm for some standard symmetric polygons, then applying them to simulations for arbitrary-shaped samples. Furthermore, the vortex-antivortex configurations of symmetric solutions obtained using our finite element analysis for the linearized Ginzburg-Landau equation together with a uniform magnetic field distribution can be used as a starting point for an iterative solution of the non-linear Ginzburg-Landau equations near the phase boundary,

which can then be used as starting point to solve the non-linear Ginzburg-Landau equations further inside the phase boundary. In this regard a very interesting question can be raised: It is well known that far away from the phase boundary vortices are not arranged to uphold the symmetry of the sample. Is this loss of symmetry gradually or suddenly turned on when H and/or T are/is lowered away from the phase boundary? This will be a subject of a future study.

Acknowledgments

The authors thank John Burkardt for help on coding issues related to the project. C.-R. Hu acknowledges partial support in the summer of 2007 from the Texas Center for Superconductivity at the University of Houston.

References

[1] M. Tinkham, Introduction to Superconductivity (McGraw-Hill, New York, 1996).
[2] P. G. de Gennes, Superconductivity in Metals and Alloys, W. A. Benjamin, New York (1966). Reprinted by Addison-Wesley, Reading, MA (1989).
[3] H. J. Fink and A. G. Presson, Phys. Rev. 151, 219 (1966).
[4] H. J. Fink and A. G. Presson, Phys. Rev. 182, 498 (1969).
[5] B. J. Baelus and F. M. Peeters, Phys. Rev. B 65 104515, (2002).
[6] V. A. Schweigert and F. M. Peeters, Phys. Rev. B 57 13817 (1998).
[7] V. A. Schweigert, F. M. Peeters, and P. Singha Deo, Phys. Rev. Lett. 81 2783 (1998).
[8] P. Singha Deo, V. A. Schweigert, F. M. Peeters, and A. K. Geim, Phys. Rev. Lett. 79 4653 (1997).
[9] W. A. Little and R. D. Parks, Phys. Rev. Lett. 9, 9 (1962).
[10] R. P. Groff and R. D. Parks, Phys. Rev. 176, 567 (1968).
[11] J. B. Ketterson and S. N. Song, Superconductivity (Cambridge University Press, Cambridge, 1999).
[12] O. Buisson, P. Gandit, R. Rammal, Y. Y. Wang, and B. Pannetier, Phys. Lett. A 150, 36 (1990).
[13] V. V. Moshchalkov, L. Gielen, C. Strunk, R. Jonckheere, X. Qiu, C. Van Haesendonck, and Y. Bruynseraede, Nature (London) 373, 319 (1995).
[14] V. V. Moshchalkov, L. Gielen, M. Baert, V. Metlushko, G. Neuttiens, C. Strunk, V. Bruyndoncx, X. Qiu, M. Dhallé, K. Temst, C. Potter, R. Jonckheere, L. Stockman, M. Van Bael, C. Van Haesendonck, and Y. Bruynseraede, Physica Scripta T55, 168 (1994).
[15] V. M. Fomin, V. R. Misko, J. T. Devreese, and V. V. Moshchalkov, Solid State Comm. 101, 303 (1997).
[16] V. M. Fomin, V. R. Misko, J. T. Devreese, and V. V. Moshchalkov, Phys. Rev. B 58, 11703 (1998).
[17] V. Bruyndoncx, J. G. Rodrigo, T. Puig, L. Van Look, and V. V. Moshchalkov, Phys. Rev. B 60, 4285 (1999).
[18] H. T. Jadallah, J. Rubinstein, and P. Sternberg, Phys. Rev. Lett. 82, 2935 (1999).
[19] L. F. Chibotaru, A. Ceulemans, V. Bruyndoncx, and V. V. Moshchalkov, Nature 408, 833 (2000).
[20] L. F. Chibotaru, A. Ceulemans, V. Bruyndoncx, and V. V. Moshchalkov, Phys. Rev. Lett. 86, 1323 (2001).

[21] L. F. Chibotaru, A. Ceulemans, V. Bruyndoncx, and V. V. Moshchalkov, Physica C 369, 149 (2002).
[22] L. F. Chibotaru, A. Ceulemans, G. Teniers, V. Bruyndoncx, and V. V. Moshchalkov, Eur. Phys. J. B 27, 341 (2002).
[23] L. F. Chibotaru, A. Ceulemans, M. Morelle, G. Teniers, C. Carballeira, and V. V. Moshchalkov, J. Math. Phys. 46, 095108 (2005).
[24] V. G. Kogan, J. R. Clem, J. M. Deang, and M. D. Gunzburger, Phys. Rev. B, 65, 094514 (2002).
[25] Q. Du, M. D. Gunzburger, J. S. Peterson, SIAM Review 34, 54, (1992).
[26] Q. Du, M. D. Gunzburger, J. S. Peterson, Phys. Rev. B 51, 16194, (1995).
[27] T. Puig, E. Rosseel, M. Baert, M. J. Van Bael, V. V. Moshchalkov, and Y. Bruynseraede, Appl. Phys. Lett. 70, 3155 (1997).
[28] T. Puig, E. Rosseel, L. Van Look, M. J. Van Bael, V. V. Moshchalkov, and Y. Bruynseraede, Phys. Rev. B 58, 5744 (1998).
[29] For a study of such non-volatile storage through vortex creation and pinning, see S. Kim, C.-R. Hu and M. J. Andrews, Phys. Rev. B 74, 214511 (2006).
[30] R. Geurts, M. V. Milošević, and F. M. Peeters, Phys. Rev. Lett. 97, 137002 (2006).
[31] S. Kim, J. Burkardt, M. Gunzburger, J. Peterson, and C.-R. Hu, Phys. Rev. B 76, 024509 (2007).
[32] O. C. Zienkiewicz, R. L. Taylor, and J. Z. Zhu, The Finite Element Method: Its Basis and Fundamentals, Elsevier Butterworth-Heinemann (2005).
[33] J. Jin, The Finite Element Method in Electromagnetics, John Wiley & Sons, Inc., New York (2002).
[34] P. Ciarlet, Finite Element Methods for Elliptic Problems, SIAM, Philadelphia, 2002.
[35] Jonathan Richard Shewchuk, "Triangle: Engineering a 2D Quality Mesh Generator and Delaunay Triangulator," in Applied Computational Geometry: Towards Geometric Engineering (Ming C. Lin and Dinesh Manocha, editors), volume 1148 of Lecture Notes in Computer Science, pages 203-222, Springer-Verlag, Berlin, May 1996. (From the First ACM Workshop on Applied Computational Geometry.)
[36] R. B. Lehoucq, D. C. Sorensen, and C. Yang, ARPACK USERS GUIDE: Solution of Large Scale Eigenvalue Problems with Implicitly Restarted Arnoldi Methods, SIAM, 1998, Phildelphia.
[37] A. S. Mel'nikov, I. M. Nefedov, D. A. Ryzhov, I. A. Shereshevskii, V. M. Vinokur, and P. P. Vysheslavtsev, Phys. Rev. B 65, 140503 (2002).
[38] D. Saint-James, G. Sarma, and E. J. Thomas, Type-II Superconductivity, Pergamon Press, Oxford (1969). Eq. (3.39).
[39] D. A. Dikin, V. Chandrasekhar, V. R. Misko, V. M. Fomin, and J. T. Devreese, Eur. Phys. J. B 34, 231 (2003).
[40] V. M. Fomin, J. T. Devreese, and V. V. Moshchalkov, Europhys. Lett. 42, 553 (1998).
[41] F. Brosens, J. T. Devreese, V. M. Fomin, and V. V. Moshchalkov, Solid State Comm. 111, 565 (1999).
[42] S. N. Klimin, V. M. Fomin, J. T. Devreese, and V. V. Moshchalkov, Solid State Comm. 111, 589 (1999).
[43] V. A. Schweigert and F. M. Peeters, Phys. Rev. B 60, 3084 (1999).
[44] A. P. van Gelder, Phys. Rev. Lett. 20 1435 (1968).
[45] P. Chaudhari and S.-Y. Lin, Phys. Rev. Lett. 72, 1084 (1994).
[46] J. Nocedal and S. J. Wright, Numerical Optimization (Springer, New York, 1999).